HAL
open science

Shape Representation and Modeling of Tendon-Driven Continuum Robots using Euler Arc Splines

Priyanka Rao, Quentin Peyron, Jessica Burgner-Kahrs

To cite this version:

Priyanka Rao, Quentin Peyron, Jessica Burgner-Kahrs. Shape Representation and Modeling of Tendon-Driven Continuum Robots using Euler Arc Splines. IEEE Robotics and Automation Letters, 2022, 7 (3), pp.8114-8121. 10.1109/LRA.2022.3185377 . hal-03899902

HAL Id: hal-03899902

https://hal.science/hal-03899902v1

Submitted on 15 Dec 2022

HAL is a multi-disciplinary open access archive for the deposit and dissemination of scientific research documents, whether they are published or not. The documents may come from teaching and research institutions in France or abroad, or from public or private research centers.

L'archive ouverte pluridisciplinaire **HAL**, est destinée au dépôt et à la diffusion de documents scientifiques de niveau recherche, publiés ou non, émanant des établissements d'enseignement et de recherche français ou étrangers, des laboratoires publics ou privés.

Shape Representation and Modeling of Tendon-Driven Continuum Robots using Euler Arc Splines

Priyanka Rao[1], *Student Member, IEEE*, Quentin Peyron[1,2], *Member, IEEE*, and Jessica Burgner-Kahrs[1], *Senior Member, IEEE*

***Abstract*—Due to the compliance of tendon-driven continuum robots, carrying a load or experiencing a tip force result in variations in backbone curvature. While the spatial robot configuration theoretically needs an infinite number of parameters for exact description, it can be well approximated using Euler Arc Splines which use only six of them. In this letter, we first show the accuracy of this representation by fitting the Euler Arc splines directly to experimentally measured robot shapes. Additionally, we propose a 3D static model that can account for gravity, friction and tip forces. We demonstrate the utility of using efficient parameterization by analyzing the computation time of the proposed model and then, using it to propose a hybrid model that combines physics-based model with observed data. The average tip error for the Euler arc spline representation is 0.43% and the proposed static model is 3.25% w.r.t. robot length. The average computation time is $0.56\,\mathrm{ms}$ for nonplanar deformations for a robot with ten disks. The hybrid model reduces the maximum error predicted by the static model from 8.6% to 5.1% w.r.t. robot length, while using 30 observations for training.**

***Index Terms*—Modeling, Control, and Learning for Soft Robots, Flexible Robotics, Kinematics.**

I. Introduction

TENDON-DRIVEN continuum robots (TDCRs) have been widely studied in recent literature due to their applications in medicine and industry. They are a class of continuum robots actuated by the pull and release of tendons routed along the backbone. Point of termination of these tendons marks the end of a segment. Due to their slender flexible backbones they can bend continuously in 3D space, allowing their use in inspecting regions with constricted entry-points. They are compliant as well, and undergo deformations when acted on by external forces. Predicting and simulating their behaviour in real-time is required for their design, planning, and control.

There are two main challenges that need to be taken into consideration while modeling TDCRs. The first is their backbone representation. Theoretically, an infinite number of parameters is required to represent the continuous backbone. The second is estimating the mapping between the actuation space to the resulting backbone shape. Both the challenges are inter-dependent and influenced by the robots elastic properties, friction interactions and acting forces.

A. Related Work

To address the first challenge, a common approach [1] is to use a curve-based description based on differential geometry. A moving frame along the backbone is used to represent its pose at any arc-length, providing a so called distributed parametrization which requires an infinite number of parameters. The robot shape is then reconstructed from its linear and angular strain using differential geometry, leading to the resolution of differential equations with mixed boundary conditions. While shown to be accurate [2], [3] and solved analytically for simple scenarios [4], they require numerical integration for the general case and can be computationally complex. An alternative is provided by the lumped backbone parameterization, where the backbone is approximated by a discrete number of variables.

One of the most common lumped parameterization is the constant curvature (CC) approach [5] where the entire segment is assumed to have a constant bending curvature. Models using the CC assumption use the minimum numbers of parameters which lead to efficient kinematic and static models [6]. However, their simplicity limits their use and they can only account for pure bending and not external forces. An extension to the above is provided by the piece-wise constant curvature assumption (PCCA) [7], [8] where the backbone is modelled as a sequence of mutually tangent circular arcs that can account for both twist and bending curvatures. In pseudo-rigid body modeling (PRBM) [9], [10], the backbone is assumed to be a series of rigid links connected by torsion springs. The model in [11] can consider any modal approximation for the backbone. In [12], the backbones curvature are modeled as polynomial functions. It is shown in [13] and [14] that Bezier and pythagorean hodograph curves respectively can be used to accurately represent the backbone shape of a TDCR. The challenge with the above representations is to select them based on the required application [15] as there is a tradeoff between accuracy and computational efficiency.

The second challenge of providing a mapping is interlinked with the first - appropriate backbone representation is used

Manuscript received: February, 18, 2022; Revised April, 26, 2022; Accepted May, 31, 2022. This letter was recommended for publication by Associate Editor F. Renda and Editor C. Laschi upon evaluation of the reviewers' comments. This work was supported in part by the Natural Sciences and Engineering Research Council of Canada (NSERC) under Grant RGPIN-2019-04846 and in part by the CREATE Healthcare in Robotics fund.

[1]The authors are with the Continuum Robotics Laboratory, Department of Mathematical & Computational Sciences, University of Toronto, ON, Canada priyankaprakash.rao@mail.utoronto.ca

[2]Quentin Peyron is also with the DEFROST Team, Inria Lille-Nord Europe and CRIStAL UMR CNRS 9189, University of Lille, Villeneuve d'Ascq, France quentin.peyron@inria.fr

Digital Object Identifier (DOI): see top of this page.

to formulate a physics-based or data-driven model, or a combination of the two. Physics-based models such as the ones formulated using the Cosserat rod theory (CRT) or beam mechanics, use the Lagrangian formulation or Newton mechanics to arrive at the static equilibrium equations. However, physical prototypes experience several phenomena that are difficult to model accurately such as manufacturing and assembly errors. These result in deviations from the solutions of physics-based models. It has been demonstrated that these errors can be significant and require additional parameters like twist in the backbone [16] to be accounted for.

An alternative to physics-based approaches is to use pure data-driven models to learn the behaviour of these robots. In [17], a data-driven model is developed to predict the end-effector position and a PRBM representation is used to estimate the rest of the backbone in 2D. A constant-curvature representation is used in [18] to learn the inverse kinematics of a multi-segment robot. While the above look at free space behaviour of continuum robots, [19] use a spline curve to represent a catheter experiencing contact forces in 2D and use measurements to characterise force acting on the catheter tip. Pure-data learning approaches require a large number of training data, even when pre-trained by a physics-based model. They cannot extrapolate as well as physics-based models, requiring careful selection of training data [20]. When there is a tip force, the required number of data points of the robot in free space is compounded by an infinite combination of possible magnitudes and direction of forces.

A compromise between physics-based and data-driven models can be obtained by combining them under hybrid modeling approaches, where the latter is used to learn the error models of physics based modeling. Its advantages are detailed in [20], which state that the complexity of the error model is lower since the analytical model captures essential behaviour, and can avoid overfitting sparse data. The authors use the CC representation for control of a TDCR and investigate different data learning approaches. Model calibration is used in [21] to account for the variations observed in a CC representation based on experimental data. Data-driven models are used to learn the position errors of a TDCR, while using a CC representation in [22], [23]. All the above works assume that the robot is operating in free space. The work in [12] uses the PCCA combined with Gaussian process regression to learn the direction of contact forces but ignores twist in the backbone. A modal based representation is used in [24] for a soft robot experiencing contact forces and uses experimental data to estimate its parameters. However this is only done for a 1-DOF system experiencing planar forces. Most of the approaches in hybrid modeling are restricted to the no-twist constant curvature assumption or the 1D case, and have not been applied to 3D deformation caused by tip forces.

B. Our Contribution

All three approaches - physics-based, data-driven, and hybrid modeling benefit from using an efficient and accurate backbone representation. This advantage is because the representation can be used to estimate the backbone shape, reduce model complexity, and reduce the number of unknown parameters and output required to be estimated by data-driven approaches. Both forward and inverse kinematics frameworks can benefit from such an approach.

Recently, the use of Euler curves has gained traction as a lumped parameterization approach, where the backbone curvature is assumed to vary linearly along the backbone. A linear curvature profile is typically obtained for cantilever beams under small deformation, subject to external point forces. As a result, the linear assumption works well for continuum robots in several application scenarios, even for large deformations. It has been used to represent the shape of slender backbones affected by gravity [25], [26], contact forces with the environment [27], and forces due to tools mounted at the tip [28]. In our previous work [28], we provide a 2D static model to model tip forces on a single segment using Euler arc splines (EAS). While Euler curves require the use of Fresnel integrals which can be computationally expensive, the use of EAS to represent the backbone shape reduces the computational complexity [29].

In this work, we extend our previous work and present the use of EAS in the forward kinematics framework for a TDCR experiencing 3D tip forces. First, we prove their efficacy in representing TDCR shapes in experimental data, whereas [28] only compared them in simulation. Next, we extend the previously proposed 2D static model to 3D that maps the input tendon tensions to corresponding backbone curvatures and can account for gravity, friction, and tip forces. The reduced model complexity is studied via an analysis of the models computation time. Finally, we demonstrate the advantage of the representation through the use of a hybrid model approach that uses a data analytics approach to learn the configuration space errors for the robot forward kinematics.

II. Efficacy of the 3D EAS representation

In this section, we evaluate the EAS representation on experimental data. First, we evaluate the efficacy of the proposed 3D EAS representation on collected experimental data. For given discrete measured position coordinates a method for fitting an Euler curve is proposed. Second, the experimental setup used to collect data and finally, the accuracy of the EAS curves compared to the data is reported.

A. 3D Euler Arc Splines

A single segment is represented by Euler arc splines (EAS) by dividing it into a series of arcs with constant curvature and torsion. The consecutive arcs have equal lengths and common tangents, forming a G^1 continuous curve, with curvatures varying in arithmetic progression [30]. A Bishop frame is attached to the base of each arc, resolving the curvature into bending and torsional components.

Consider a continuum backbone of constant length ℓ, represented as an Euler curve in 3D. The EAS approximation in [30] is extended to 3D, by applying the linear curvature assumption to the bending and torsional components. The bending curvature components along the $\mathbf{x}$ and $\mathbf{y}$ axes are denoted by κ_x and κ_y and the torsional component about the

$\mathbf{z}$ axis, representing the twist about the backbone is denoted by τ. The backbone is divided into n arcs of equal length, where $\ell_i = \ell/n$ for all $i = 1, 2..n$. The vector $\boldsymbol{u}_i$ represents the curvature components for arc i.

$$\boldsymbol{u}_i = \boldsymbol{u}_1 + (\boldsymbol{u}_n - \boldsymbol{u}_1)\frac{(i-1)}{(n-1)} \tag{1}$$

$$\boldsymbol{u}_i = \left[\kappa_{i,x}, \kappa_{i,y}, \tau_i\right]^\top \tag{2}$$

The x and y components of bending curvature can be alternatively expressed in terms of curvature κ and angle ϕ made by the bending plane with the $\mathbf{x}$ axis

$$\kappa_i = \sqrt{\kappa_{i,x}^2 + \kappa_{i,y}^2} \tag{3}$$

$$\phi_i = \operatorname{atan2}(\kappa_{i,y}, \kappa_{i,x}) \tag{4}$$

Following the convention in [5] and [8], a local reference frame $\mathbf{R}_i$ is attached to the base of each arc at O_i, with the local z-axis always tangent to the backbone. The homogeneous transformation from R_i to R_{i-1} is given by the transformation matrix $T_{i-1}^i \in \mathrm{SE}(3)$.

$$\mathbf{T}_i^{i-1} = \begin{bmatrix} \mathbf{R}_z(\phi_i)\mathbf{R}_y(\kappa_i\ell_i)\mathbf{R}_z(\tau_i\ell_i - \phi_i) & \mathbf{p}_i \\ \mathbf{0} & 1 \end{bmatrix} \tag{5}$$

$$\mathbf{p}_i = \begin{bmatrix} \frac{\cos\phi_i}{\kappa_i}(1 - \cos(\kappa_i\ell_i)) \\ \frac{\sin\phi_i}{\kappa_i}(1 - \cos(\kappa_i\ell_i)) \\ \frac{1}{\kappa_i}\sin(\kappa_i\ell_i) \end{bmatrix} \tag{6}$$

where $\mathbf{R}_h(\delta)$ represents rotation about axis h by δ. The corresponding points and coordinate frames are depicted in Fig. 3. We can obtain the transformation matrix between the reference frames at disk i and j, where $i > j$, as

$$\mathbf{T}_i^j = \prod_{l=j+1}^{i} \mathbf{T}_l^{l-1} \tag{7}$$

Discretizing the backbone into CC arcs avoids the calculation of Fresnel integrals for backbone reconstruction and simplifies the configuration to task space mapping, reducing its computational complexity as it only requires matrix multiplications.

B. Experimental Setup and Data Collection

Two sets of data were collected from two differently oriented prototypes, shown in Fig. 1. A Nitinol rod of length $134\,\mathrm{mm}$ and diameter $0.99\,\mathrm{mm}$ acts as the central backbone for both prototypes. Each consists of nine 3D printed disks with a spherical cap in their center. Three tendons are placed around the backbone at a distance of $7\,\mathrm{mm}$. Braided ropes (KastKing, New York , USA) of diameter $0.17\,\mathrm{mm}$ are used as tendons. A FARO Edge ScanArm (FARO Technologies, Florida, USA), of accuracy $\pm 0.041\,\mathrm{mm}$ is used to scan the point-cloud of each disk and spheres of diameter $7\,\mathrm{mm}$ are fit manually to the spherical cap using the FARO CAM2® software. The centers of these spheres are returned as the coordinates of each disk. For set 1, two additional metallic spheres, shown in Fig. 1, are scanned to measure the direction of the external force $\mathbf{F}_e$.

In set 1, the robot is oriented vertically, such that the local z-axis at the base of the robot is parallel to the direction of gravity. In this set, 40 measurements are made both with no-load and load acting on the tip. For loaded measurements, both the force magnitude $(0 - 50\,\mathrm{g})$ and direction is varied randomly. The force is applied by hanging a mass over a pulley by a tendon fixed at the tip. A mass of $50\,\mathrm{g}$ induces significant backbone out-of-plane tip deflections of $45°$. The direction is varied by vertically moving the rail on which the pulley is placed as well as by moving the entire rail in random coordinates. In addition, the tensions in the tendons are varied randomly as well. Set 2 consists of loaded measurements only, each of constant magnitude $30\,\mathrm{g}$ and was collected to reflect the case where the TDCR is bearing a load. The robot is oriented horizontally such that the local z-axis is parallel to the ground. In each reading, the load at the tip is simply left hanging such that the direction is always parallel to the direction of gravity. Due to the lower number of varying factors, 30 measurements were taken.

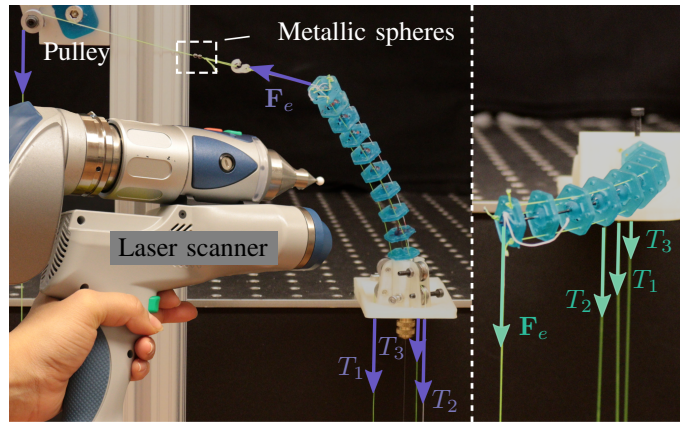

Fig. 1. Experimental setup for the data collection of set 1 (left) and set 2 (right). The base of the prototypes are oriented perpendicular and parallel to the direction of gravity respectively. The FAROArm is used to scan the 3D point cloud of the disks. Two metallic spheres are scanned in addition in set 1 to determine the direction of external force $\mathbf{F}_e$. Tendon tensions (T_1, T_2, T_3) are applied by hanging calibrated weights.

C. Shape Reconstruction Method

The input to the reconstruction method is the set of points $\mathbf{P} = \{\mathbf{x}_k | k \in M\}$, where M denotes the set of indices of the measured disks. The measured index can be replaced by the set of arc lengths along which measurements are made if disk positions are not used. For these positions are measured along the backbone, the objective function needs to minimize their Euclidean distance with the positions obtained from the EAS representation. We take inspiration from [31] and [32] that use minimal energy curves to represent stable curves in 3D. To do so, we minimize both curvature and torsion along with the Euclidean distances. The corresponding objective function is

$$\min_{(\mathbf{u}_1, \mathbf{u}_n)} \quad \sum_k^M \left(||\mathbf{x}_k - O_k||\right)^2 + \lambda\left(\mathbf{u}_1^\top\mathbf{u}_1 + \mathbf{u}_n^\top\mathbf{u}_n\right) \tag{8}$$

where λ is a weighting factor.

The values are calculated by optimising the objective function (8) using Nelder-Mead Simplex method implemented in MATLAB's *fminsearch* function.

D. Evaluation of the reconstructed curves

To evaluate the efficacy of 3D EAS, we calculate the optimum $\mathbf{u_1}$ and $\mathbf{u_n}$ values for 70 ground truth measurements. The errors are measured as the Euclidean distance between the measured data points and the corresponding positions along the EAS defined by $\mathbf{u}_1$ and $\mathbf{u}_n$. We consider here that the number of EAS used is equal to the number of disks, such that the portion of the backbone between two disks corresponds to a constant curvature arc. The value of λ is set as 10^{-7} empirically since the measurements are in the mm range and all quantities are expressed in meters.

The position of the nine disks along the fitted curves, such that $M = \{1, 2..9\}$ are plotted against the measured data points in Fig. 2(a) and (b) for set 1 and 2 respectively. The initial guess is assumed to be a constant curvature arc whose tip coincides with the end-effector disk [5]. The corresponding average and standard deviation of the errors in the two sets are plotted in Fig. 2(c). The average tip error of the end disk over the 70 observations is $0.43 \pm 0.21\%$ w.r.t length or $0.58 \pm 0.28\mathrm{mm}$. The error in tip position remains well within 1% for both sets. We see that the errors are consistently high for disk 2, even though higher indices have lower error. This error can be explained by the inaccuracies in the tool used to align and assemble the disks on the backbone, resulting in unequal inter-disk distances.

E. Discussion

We observe experimentally that 3D EAS can be used to accurately represent the shape of a one segment TDCR subject to tip forces with straight tendon routing while using six parameters. In comparison, the average error in reconstruction using Bézier curves for loaded configurations is reported as 2.24% w.r.t. length [13] and requires at least nine parameters per segment. Use of quintic Pythagorean Hodograph curves require the determination of six control points. Since the base and its orientation is fixed, four control points, each with three parameters, need to be estimated. An average shape error of $4\,\mathrm{mm}$ is reported [14] for configurations of around $300\,\mathrm{mm}$ length for an extensible robot. The linear curvature assumption is a simplified case of the PCCA representation. However, the linear curvature assumption restricts and reduces the configuration space of the continuous backbone from $3n$ to six curvature parameters $[\mathbf{u}_1, \mathbf{u}_n]$. Its dimensionality reduction offers advantages for design optimisation or machine-learning approaches. In our case, it motivates the development of an efficient 3D static model of a TDCR.

III. Proposed 3D EAS Model

The static model is used to obtain the curvatures $\mathbf{u}_1$ and $\mathbf{u}_n$, composed of parameters $[\kappa_{1,x}, \kappa_{1,y}, \tau_1, \kappa_{n,x}, \kappa_{n,y}, \tau_n]$, for given tendon tensions and applied external force. A subsegment i consists of the portion of backbone between disks $i-1$ and i, including disk i. The static equilibrium equations are written for each subsegment, i w.r.t the frame of reference of disk $i-1$. We assume that the backbone is inextensible and that the tendon is always pulled unidirectionally. Therefore, the experienced shear and hysteresis are assumed to be negligible. The disks are assumed to have negligible thickness.

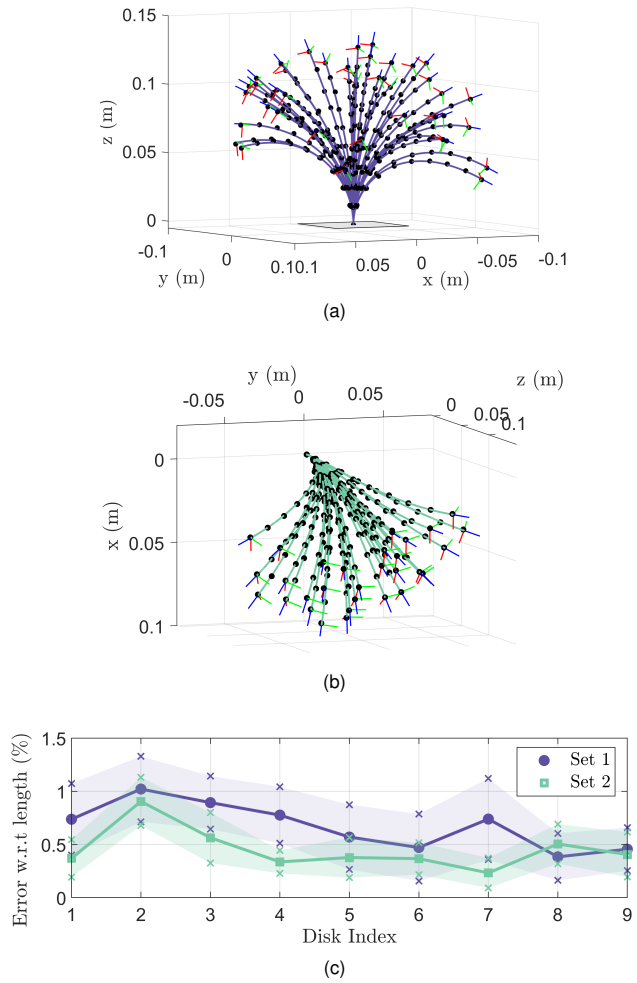

Fig. 2. Plot of the fitted curve shown in color, against the experimental data denoted by black points, for (a) Set 1 and (b) Set 2. The corresponding frame attached to the end-effector of each configuration is plotted with red, blue, green denoting the local x, y and z axis respectively. (c) Plot of the mean (solid line) and standard deviation (marked by 'x') of the Euclidean distance between measured and fitted EAS curve, expressed w.r.t. backbone length, plotted for each of the 9 disks in the two sets

A. Tendon interactions and acting forces

The m tendons are distributed equidistantly around the backbone at a distance of r_d. The position vector of tendon k at disk i, ${}^iP_{i,k}$, expressed w.r.t. the reference frame attached to the disk i are given by

$$ {}^i\mathbf{p}_{t,(i,k)} = \overrightarrow{{}^iO_i\,{}^iP_{i,k}} = r_d \begin{bmatrix} \cos(\sigma_k) & \sin(\sigma_k) & 0 \end{bmatrix}^\top \tag{9} $$

where $k \in [1, 2, ..m]$ and the angle σ_k is measured with respect to the x axis and is equal to $2\pi(k-1)/m$. The unit vector between two tendon positions in the ith frame, $(\overrightarrow{{}^iP_{i,k}\,{}^iP_{i-1,k}})/||\overrightarrow{{}^iP_{i,k}\,{}^iP_{i-1,k}}||$ is denoted by ${}^i\hat{\mathbf{t}}_{k,(i-1,i)}$. We assume that the tendons are partially constrained [15]. The forces and moments due to tendon k at disk i are given by

$$ {}^{i-1}\mathbf{F}_{i,k} = F_{i,k}\,{}^{i-1}\hat{\mathbf{t}}_{k,(i-1,i)} + F_{i+1,k}\,{}^{i-1}\hat{\mathbf{t}}_{k,(i+1,i)} \tag{10} $$

$$ {}^{i-1}\mathbf{M}_{i,k} = {}^{i-1}\mathbf{p}_{t,(i,k)} \times {}^{i-1}\mathbf{F}_{i,k} \tag{11} $$

When i is equal to n, the above force equation reduces to

$$ {}^{n-1}\mathbf{F}_{n,k} = F_{i,k}\,{}^{n-1}\hat{\mathbf{t}}_{k,(n-1,n)} \tag{12} $$

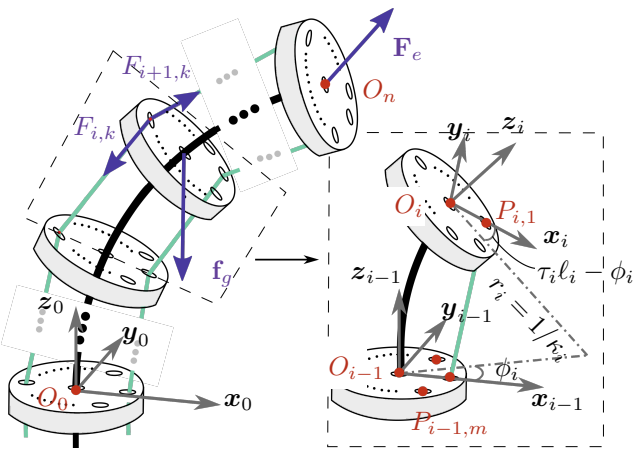

Fig. 3. Diagrammatic representation of the TDCR structure on the left, consisting of n disks. External force $\mathbf{F}_e$ acts on disk n. Some of the local forces acting on subsegment i are marked - $F_{i,k}$ and $F_{i+1,k}$ denote the magnitudes of the tendon force on tendon k. The weight of disk i is denoted by $\mathbf{f}_g$. The inset marks the subsegment i kinematics, with the base at disk positions O_{i-1} and tip at O_i, with corresponding frames attached to them. The m tendons are arranged in an anti-clockwise manner, with $P_{i,k}$ denoting the position of the kth tendon at disk i.

The variables $F_{i,k}$ and $F_{i+1,k}$ represent the magnitude of tension experienced by the tendon. This tension varies along the backbone due to the friction between the tendons and the disks. As done in [7], we assume that the frictional force can be estimated using the Coulomb friction model. The net normal force acting on the disk due to the tendon forces can be obtained by subtracting the component of force along the z_i-axis. We also consider the tendon sliding direction to always be from $i+1$ to the ith disk. The resulting tension magnitude $F_{i+1,k}$ can be calculated as

$$F_{i+1,k} = F_{i,k} - \mu|{}^{i-1}\mathbf{N}_{i,k}| \tag{13}$$

$${}^{i-1}\mathbf{N}_{i,k} = {}^{i-1}\mathbf{F}_{i,k} - \left({}^{i-1}\mathbf{F}_{i,k}^{\top}\,{}^{i-1}\mathbf{z}_i\right){}^{i-1}\mathbf{z}_i. \tag{14}$$

Following the above, we calculate the force due to gravity of disk i by transforming the weight ${}^0\mathbf{f}_g$ of the disk to the local frame, and the corresponding moment as

$${}^{i-1}\mathbf{F}_{g,i} = {}^{i-1}\mathbf{T}_0\,{}^0\mathbf{f}_g \tag{15}$$

$${}^{i-1}\mathbf{M}_{g,i} = {}^{i-1}\mathbf{p}_i \times {}^{i-1}\mathbf{F}_{g,i} \tag{16}$$

Similarly, the forces and moments due to the external force can be written as

$${}^{n-1}\mathbf{F}_{ext} = {}^{n-1}\mathbf{T}_0\,{}^0\mathbf{F}_e \tag{17}$$

$${}^{n-1}\mathbf{M}_{ext} = {}^{n-1}\mathbf{p}_n \times {}^{n-1}\mathbf{F}_e \tag{18}$$

where $\mathbf{F}_e$ denotes the external vector expressed in the global frame. The net force and moment at each subsegment is given by

$${}^{i-1}\mathbf{F}_i = \sum_k^m {}^{i-1}\mathbf{F}_{i,k} + {}^{i-1}\mathbf{F}_{g,i} + {}^{i-1}\mathbf{F}_{i+1} \tag{19}$$

$${}^{i-1}\mathbf{M}_i = \sum_k^m {}^{i-1}\mathbf{M}_{i,k} + {}^{i-1}\mathbf{M}_{g,i} + {}^{i-1}\mathbf{p}_i \times {}^{i-1}\mathbf{F}_{i+1} \tag{20}$$

When $i = n$, ${}^{n-1}\mathbf{F}_{ext}$ and ${}^{n-1}\mathbf{M}_{ext}$ must be added to the equilibrium equations.

B. Constitutive equations

Using Hooke's law, the constitutive equation for subsegment i can be calculated by relating the resultant moment to the corresponding material properties as

$${}^{i-1}\mathbf{M}_i = \mathbf{R}_z(\phi_i)\mathbf{R}_y(\kappa_i\ell_i)\begin{bmatrix} EI & 0 & 0 \\ 0 & EI & 0 \\ 0 & 0 & GJ \end{bmatrix}\begin{bmatrix} 0 \\ \kappa_i \\ \tau_i \end{bmatrix} \tag{21}$$

where I denotes the second area moments, J the polar second moment of cross sectional area, and E and G the Youngs and shear modulus. The values κ_i and ϕ_i can be obtained from (3) and (4). Isolating the bending and torsional components of moment, we can express the bending moment of each subsegment using (21) as

$$\begin{bmatrix} 0 \\ EI\kappa_i \\ GJ\tau_i \end{bmatrix} = \mathbf{R}_i^{-1}\left({}^{i-1}\mathbf{M}_i\right) \tag{22}$$

$$\mathbf{R}_i = \mathbf{R}_z(\phi_i)\mathbf{R}_y(\kappa_i\ell_i) \tag{23}$$

Since the left hand side of the equation is composed of linear curvature components, we need to project the components of moments in the right hand side of the equation to be linear as well. As done in [28], we use closed form solution of least squares linear regression to obtain the vector of linearly varying component of the experienced moment. Assembling the moment vectors for n subsegments in (22) into a matrix gives us $\mathbf{M} = \left[\mathbf{R}_1^{-1}\left({}^0\mathbf{M}_1\right) \;\; \dots \;\; \mathbf{R}_i^{-1}\left({}^{i-1}\mathbf{M}_i\right) \;\; \dots \;\; \mathbf{R}_n^{-1}\left({}^{n-1}\mathbf{M}_n\right)\right]$, which is a $n \times 3$ matrix. The linearized components are given by $\overline{\mathbf{M}}$

$$\overline{\mathbf{M}} = \mathbf{A}\mathbf{B} \tag{24}$$

$$[\mathbf{A}]_{i,} = \begin{bmatrix} 1 & i \end{bmatrix} \tag{25}$$

$$\mathbf{B} = (\mathbf{A}^T\mathbf{A})^{-1}\mathbf{A}^T\mathbf{M} \tag{26}$$

where $\mathbf{A}$ is a $n \times 2$ matrix and $\mathbf{B}$ is a 2×3 matrix of coefficients. Using the rows 1 and n, $\overline{\mathbf{m}}_1$ and $\overline{\mathbf{m}}_n$ of $\overline{\mathbf{M}}$, we obtain the 6 nonlinear equations we need to solve.

$$\begin{bmatrix} \overline{\mathbf{m}}_1^{\top} & \overline{\mathbf{m}}_n^{\top} \end{bmatrix} = \begin{bmatrix} 0 & EI\kappa_1 & GJ\tau_1 & 0 & EI\kappa_n & GJ\tau_n \end{bmatrix} \tag{27}$$

C. Numerical Solution and Computation Time

The EAS model is implemented in C++ using the framework in [15] on an Intel Core i5-9600 CPU running at 3.10 GHz. The computation time is compared with the models proposed in [7] (PCCA) and [2] (CRT). The average values over 500 configurations is computed for varying number of subsegments in a robot of length $0.134\,\mathrm{m}$. For each configuration, a random value of tension T_1 is applied such that the robot bends in the xz plane. The computation time is observed for two cases - planar and non-planar external forces. For the planar case, a force is applied along the z-axis with a randomly selected magnitude. For the non-planar case, a random magnitude of force is applied along the y-axes.

The observed computation times are plotted in Fig. 4 (a) and (b) for the planar and non-planar case for the three models.

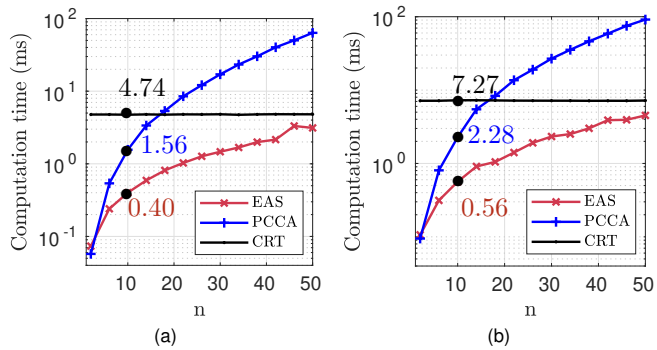

Fig. 4. Evolution of computation time of three models- EAS (red), CRT (black), and PCCA (blue) with number of disks, n for (a) planar and (b) non-planar deformations. Values for $n = 10$ are reported in the insert boxes.

The computation times for the planar case are lower than the non-planar as the twist component remains zero.

The partially constrained tendons in PCCA and EAS result in increase in the computation time with increasing number of disks, while the fully constrained model considered in CRT result in constant values. Additionally, PCCA requires the longest time with $3n$ unknowns. The increase in EAS model is due to the force equilibrium equations written at each disk. Nonetheless, the constant number of six unknowns effectively results in lower computation time. The model reports lower computation time than CRT even when considering 50 disks, and can be applied to model longer designs.

IV. Hybrid Data-Driven and Analytical Approach

In this section, we propose a hybrid model that combines the analytical static model proposed in the previous section with a data-driven error model. Since the EAS have been shown to accurately represent the shape of the backbone, we use an error model that predicts the error between the values of $\mathbf{u}^m$ predicted by the analytic model and the values observed in experimental data $\mathbf{u}^e$.

There are multiple sources of errors in the predicted values in a system model. A major factor is parameter uncertainty, where the exact value of some of the input parameters to the above static model are unknown. For example, some parameters can be subject to significant variability w.r.t. their nominal value, such as the Young modulus of Nitinol, or the friction coefficient which can vary depending on the material used, surface quality and the environment (temperature, humidity, etc). A common approach [2] is to optimise for these parameters using observed experimental data. Calibration parameters consist of values that are not directly measured in the experiment but are constant throughout the duration of the experiments [33]. Another source of errors is the model discrepancy, which accounts for errors in the model predictions due to unmodeled phenomena, like errors in assembly and manufacturing. A third source is the error in the measurement system. The system is represented by [34]

$$\mathbf{u}^e = \mathbf{u}^m + \boldsymbol{\delta}(\mathbf{v}) + \epsilon \tag{28}$$

$$\mathbf{u}^m = f(\mathbf{g}, \boldsymbol{\Theta}) \tag{29}$$

TABLE I
Average error and standard deviation of the end-effector position error as % w.r.t. length for the EAS, PCCA [7] and CRT-based model [2]

	EAS model	PCCA model	CRT model
Set 1	3.59 ± 3.36	3.68 ± 3.08	5.46 ± 4.02
Set 2	2.75 ± 1.64	2.15 ± 1.02	3.27 ± 2.14

where $\mathbf{u}^m$ is a function of input parameters $\mathbf{g}$ and calibration parameters $\boldsymbol{\Theta}$. The function $f(\mathbf{g}, \boldsymbol{\Theta})$ denotes the proposed EAS model in the previous section for input values $\mathbf{g}$ of different tensions and applied forces. Variable $\boldsymbol{\epsilon}$ represents the noise in the system. The vector $\mathbf{v}$ represents the inputs to the discrepancy function, $\boldsymbol{\delta}$ independent of $\mathbf{g}$.

We first report the errors for the above model, assuming model discrepancy is negligible. This calibration approach is being followed by majority of works in literature and the corresponding error of the proposed model is reported and compared to state-of-the-art. Next, we consider that the model discrepancy is a linear function of input features for simplicity. We then report the method and errors for the hybrid model that considers model discrepancy in addition to calibration. While any physics-basics model can be used, the efficient EAS backbone representation allows for fewer number of unknown parameters.

A. Calibration

In addition to the Youngs modulus and coefficient of friction, we calibrate the base of the robot frame as it is not exactly oriented with that of the measurement system. To align the two correctly, we rotate the observed experimental data about the x, y, and z axes, by pre-multiplying the coordinates by $\mathbf{R}^c$, where $\mathbf{R}^c = \mathbf{R}_x(\theta_x)\mathbf{R}_y(\theta_y)\mathbf{R}_z(\theta_z)$. To simplify the process, we perform standard calibration by estimating $\boldsymbol{\Theta}$ assuming there is no discrepancy [34]. The corresponding problem can be solved as a least-squares optimization, minimizing the Euclidean distance between the predicted and measured disk coordinates as

$$\min_{\boldsymbol{\Theta}} \sum_{i=1}^{n} \left(||\mathbf{x}_i - O_i||\right)^2 \tag{30}$$

$$\boldsymbol{\Theta} = \begin{bmatrix} E & \theta_x & \theta_y & \theta_z & \mu \end{bmatrix} \tag{31}$$

The resulting optimization was solved using the Nelder-Mead Simplex Method.

B. Experimental results with Calibrated model

The error performance of the EAS model, using the calibrated parameters is tabulated in Table I. The average error over the 70 measurements is $3.25 \pm 2.77\%$ w.r.t. robot length for the ninth disk. The average for set 1 is slightly higher than set 2 and can be explained by the fact that set 1 has a wider variation in force magnitude and direction, while set 2 consists of unidirectional constant force, allowing better calibration. The lesser number of varying factors is reflected in the lower standard deviation of set 2.

We also compare our model with CRT [2] which does not consider friction. The same calibration is performed by excluding μ from $\boldsymbol{\theta}$. The reported errors are on the higher range as friction plays a significant role in these experiments. The prototype experiences high tensions and large non-planar bending, resulting in larger deviations from predicted shapes due to friction. In addition, we compare the performance of the proposed model with a PCCA model [7], which accounts for friction. Here, the backbone is similarly divided into arcs of equal length but each of them is allowed to vary individually without constraints. We do so to investigate the influence of the linear approximation on the error statistics, since the force equilibrium equations remain the same. The model is again calibrated using (30). Both EAS and PCCA models provide similar accuracy. Consequently, the linear approximation does not introduce large errors in the static model.

C. Hybrid model (Model Discrepancy)

We see that even with model calibration, there remain errors in the system due to reasons such as misalignment in disks leading to twist in the backbone [21] or manufacturing errors. These errors can be further compensated by learning the discrepancy from experimental data. When calibration and model discrepancy is accounted for in addition to the model predictions, we refer to it as the hybrid EAS model in the following. We use a data-driven approach to model the discrepancy. While a variety of data analytic approaches can be chosen, for simplification we assume that the error between the curvatures is a linear combination of the input features.

$$\overline{\mathbf{u}^e} = \mathbf{u}^m + \sum_{j=1}^{p} \mathbf{w}_j \mathbf{x}_j \tag{32}$$

where $\mathbf{x}_j$ is an input feature vector of N observations and $\mathbf{w}_j$ is the corresponding weight associated with it. The objective function (30) is chosen to minimise the position error for all disks. Using the predicted value of the curvature the function (30) is then minimized using nonlinear least squares. The experiments are divided into training and test sets, such that the calibration and training is performed on the former. The training data sets are of size 30 and 20 for sets 1 & 2.

The three components of the applied tension and external force are selected as the input features along with the torsional curvature component predicted by the static model. We do so because it has been shown that twist plays a significant role in deviations from model predictions [16], [35] and is an indicator of out-of-plane deformations which in result in larger deviations from the model. The input feature vectors for set 1 are selected as $[\tau_1^m, (\tau_1^m)^2, \tau_n^m, (\tau_n^m)^2, \mathbf{F}_e^\top, F_1, F_2, F_3]$, where F_k represents the applied tension on the kth tendon. For set 2, the external force components are removed from the input vector since it remains constant. Matlab's trust-region-reflective least-squares method is used to perform the optimisation.

D. Experimental Results with Hybrid EAS model

With the calibrated parameters, we train the discrepancy model on the training data. The resulting errors of the test data is presented in Fig. 5 and Table II for both sets. We see that even with the simple model chosen, the maximum error for the last disk reduces by 3.5% w.r.t length ($4.69\,\mathrm{mm}$) for set 1 using only 30 observations for training and by 1.85% w.r.t length ($2.46\,\mathrm{mm}$) for set 2 with 20 observations.

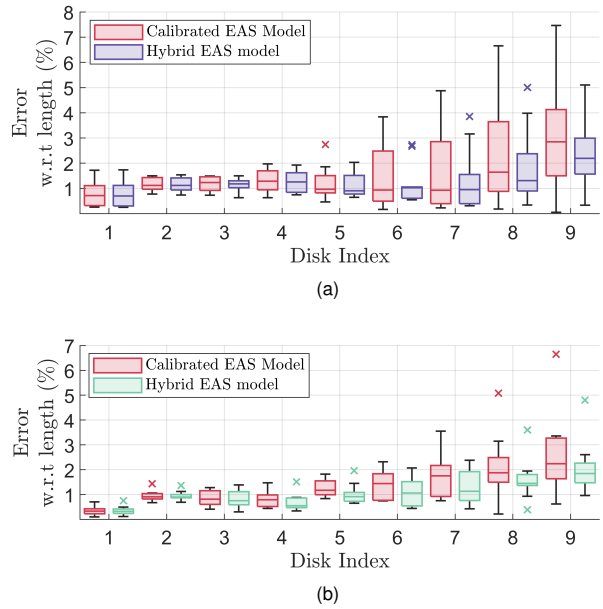

Fig. 5. Box plots of disk position errors over the test set for calibrated model (red) and hybrid model for (a) set 1 (purple) and (b) set 2 (green), reporting the 25th and 75th percentiles.

TABLE II
ERROR STATISTICS OF THE END-EFFECTOR POSITION ERROR FOR THE CALIBRATED AND HYBRID EAS MODEL FOR 10 CONFIGURATIONS

	Set 1, % w.r.t. length		Set 2, % w.r.t. length	
	Calibrated	Hybrid	Calibrated	Hybrid
Average	3.37	2.72	2.44	1.59
Standard deviation	2.64	1.63	2.05	1.10
Minimum	0.05	0.34	0.61	0.96
Maximum	8.60	5.10	6.65	4.8

The proposed model is a first step towards combining the proposed static model with observed data. While there is error reduction, using a larger dataset combined with a more sophisticated discrepancy model might result in larger improvements. Investigating the above thoroughly is beyond the scope of this letter and will be investigated in future works. An important factor in learning the forward kinematics with applied external forces is to have sufficient samples that reflect the true nature of the workspace, accounting for different direction and magnitudes of forces. Doing so efficiently without the need to collect an exhaustive amount of data is a challenge to be addressed in future works.

V. CONCLUSIONS

In this letter, we presented an EAS based 3D static model for TDCRs experiencing forces at the tip. First, the efficacy of EAS in representing backbone shapes was shown through experimental data, with an average tip error of $0.43 \pm 0.21\%$. Second, a physics-based 3D static model was presented that models the physical phenomena of the deforming TDCR with

an accuracy of $3.25 \pm 2.77\%$ w.r.t. length. Third, a formulation was proposed to improve the model accuracy by combining the proposed model with observed data. The proposed hybrid model resulted in a reduction in the maximum error by 3.5% w.r.t. length. The average computation time is $0.56\,\mathrm{ms}$ if the segment has ten disks.

The EAS representation offer the advantage of dimensionality reduction that could be useful for design optimisation, path planning, and control. It can be used in data-driven approaches for both forward and inverse kinematics. While this letter looks at only tip forces, extending it to multiple forces along the backbone can be performed using a combination of linear curves, as done in [27]. In addition, we show their efficacy only for straight routing and assume that the tendon is always pulled, which does not account for hysteresis [36]. The above constitutes an interesting topic for future work.

Acknowledgments

The authors would like to thank Reinhard Grassmann, Vincent Modes, and Vedasri Godavarthi for discussions aiding in the conceptualisation of this letter.

References

[1] H. B. Gilbert, "On the mathematical modeling of slender biomedical continuum robots," *Frontiers in Robotics and AI*, vol. 8, 2021.

[2] D. C. Rucker and R. J. Webster, "Statics and dynamics of continuum robots with general tendon routing and external loading," *IEEE Transactions on Robotics*, vol. 27, no. 6, pp. 1033–1044, 2011.

[3] F. Renda, V. Cacucciolo, J. Dias, and L. Seneviratne, "Discrete cosserat approach for soft robot dynamics: A new piece-wise constant strain model with torsion and shears," in *IEEE/RSJ International Conference on Intelligent Robots and Systems*, 2016, pp. 5495–5502.

[4] K. Xu and N. Simaan, "Analytic Formulation for Kinematics, Statics, and Shape Restoration of Multibackbone Continuum Robots Via Elliptic Integrals," *Journal of Mechanisms and Robotics*, vol. 2, no. 1, 11 2009.

[5] R. J. Webster and B. A. Jones, "Design and kinematic modeling of constant curvature continuum robots: A review," *International Journal of Robotics Research*, vol. 29, no. 13, pp. 1661–1683, 2010.

[6] D. B. Camarillo, C. F. Milne, C. R. Carlson, M. R. Zinn, and J. K. Salisbury, "Mechanics modeling of tendon-driven continuum manipulators," *IEEE Transactions on Robotics*, vol. 24, no. 6, pp. 1262–1273, 2008.

[7] H. Yuan, L. Zhou, and W. Xu, "A comprehensive static model of cable-driven multi-section continuum robots considering friction effect," *Mechanism and Machine Theory*, vol. 135, pp. 130–149, 2019.

[8] W. S. Rone and P. Ben-Tzvi, "Continuum Robot Dynamics Utilizing the Principle of Virtual Power," *IEEE Transactions on Robotics*, vol. 30, no. 1, pp. 275–287, 2014.

[9] K. P. Ashwin and A. Ghosal, "Forward Kinematics of Cable-Driven Continuum Robot Using Optimization Method," *Mechanism and Machine Science*, pp. 391–403, 2021.

[10] S. Huang, D. Meng, X. Wang, B. Liang, and W. Lu, "A 3D Static Modeling Method and Experimental Verification of Continuum Robots Based on Pseudo-Rigid Body Theory," in *IEEE International Conference on Intelligent Robots and Systems*, 2019, pp. 4672–4677.

[11] F. Renda, C. Armanini, V. Lebastard, F. Candelier, and F. Boyer, "A Geometric Variable-Strain Approach for Static Modeling of Soft Manipulators With Tendon and Fluidic Actuation," *IEEE Robotics and Automation Letters*, vol. 5, no. 3, pp. 4006–4013, 2020.

[12] C. D. Santina, R. L. Truby, and D. Rus, "Data-Driven Disturbance Observers for Estimating External Forces on Soft Robots," *IEEE Robotics and Automation Letters*, vol. 5, no. 4, pp. 5717–5724, 2020.

[13] S. Song, Z. Li, H. Yu, and H. Ren, "Electromagnetic Positioning for Tip Tracking and Shape Sensing of Flexible Robots," *IEEE Sensors Journal*, vol. 15, no. 8, pp. 4565–4575, 2015.

[14] I. Singh, Y. Amara, A. Melingui, P. Mani Pathak, and R. Merzouki, "Modeling of continuum manipulators using pythagorean hodograph curves," *Soft Robotics*, vol. 5, no. 4, pp. 425–442, 2018.

[15] P. Rao, Q. Peyron, S. Lilge, and J. Burgner-Kahrs, "How to Model Tendon-Driven Continuum Robots and Benchmark Modelling Performance," *Frontiers in Robotics and AI*, vol. 7, p. 223, 2021.

[16] L. Wang and N. Simaan, "Investigation of Error Propagation in Multi-backbone Continuum Robots," in *Advances in Robot Kinematics*. Springer International Publishing, 2014, pp. 385–394.

[17] S. Sefati, C. Gao, I. Iordachita, R. H. Taylor, and M. Armand, "Data-driven shape sensing of a surgical continuum manipulator using an uncalibrated fiber bragg grating sensor," *IEEE Sensors Journal*, vol. 21, no. 3, pp. 3066–3076, 2021.

[18] J. Lai, K. Huang, and H. K. Chu, "A learning-based inverse kinematics solver for a multi-segment continuum robot in robot-independent mapping," in *IEEE International Conference on Robotics and Biomimetics*, 2019, pp. 576–582.

[19] M. Khoshnam and R. V. Patel, "Estimating contact force for steerable ablation catheters based on shape analysis," in *IEEE/RSJ International Conference on Intelligent Robots and Systems*, 2014, pp. 3509–3514.

[20] R. F. Reinhart, Z. Shareef, and J. J. Steil, "Hybrid Analytical and Data-Driven Modeling for Feed-Forward Robot Control," *Sensors*, vol. 17, no. 2, p. 311, 2017.

[21] L. Wang and N. Simaan, "Geometric Calibration of Continuum Robots: Joint Space and Equilibrium Shape Deviations," *IEEE Transactions on Robotics*, vol. 35, no. 2, pp. 387–402, 2019.

[22] W. Shen, G. Yang, T. Zheng, Y. Wang, K. Yang, and Z. Fang, "An accuracy enhancement method for a cable-driven continuum robot with a flexible backbone," *IEEE Access*, vol. 8, pp. 37 474–37 481, 2020.

[23] R. A. Porto, F. Nageotte, P. Zanne, and M. d. Mathelin, "Position control of medical cable-driven flexible instruments by combining machine learning and kinematic analysis," in *International Conference on Robotics and Automation*, 2019, pp. 7913–7919.

[24] Y. Chen, L. Wang, K. Galloway, I. Godage, N. Simaan, and E. Barth, "Modal-based kinematics and contact detection of soft robots," *Soft Robotics*, vol. 8, no. 3, pp. 298–309, 2021.

[25] P. S. Gonthina, A. D. Kapadia, I. S. Godage, and I. D. Walker, "Modeling variable curvature parallel continuum robots using euler curves," in *IEEE International Conference on Robotics and Automation*, 2019, pp. 1679–1685.

[26] J. Fan, E. D. Dottore, F. Visentin, and B. Mazzolai, "Image-based approach to reconstruct curling in continuum structures," in *IEEE International Conference on Soft Robotics*, 2020, pp. 544–549.

[27] O. Al-Ahmad, M. Ourak, J. Vlekken, and E. Vander Poorten, "FBG-Based Estimation of External Forces Along Flexible Instrument Bodies," *Frontiers in Robotics and AI*, vol. 8, pp. 1–12, 2021.

[28] P. Rao, Q. Peyron, and J. Burgner-Kahrs, "Using euler curves to model continuum robots," in *IEEE International Conference on Robotics and Automation*, 2021, pp. 1402–1408.

[29] D. S. Meek and D. J. Walton, "An arc spline approximation to a clothoid," *Journal of Computational and Applied Mathematics*, vol. 170, no. 1, pp. 59–77, sep 2004.

[30] H. Zhou, J. Zheng, and X. Yang, "Euler arc splines for curve completion," in *Computers and Graphics (Pergamon)*, vol. 36, no. 6. Elsevier Ltd, 2012, pp. 642–650.

[31] K. Zanganeh and J. Angeles, "The inverse kinematics of hyper-redundant manipulators using splines," in *IEEE International Conference on Robotics and Automation*, 1995, pp. 2797–2802.

[32] M. Moll and L. E. Kavraki, "Path planning for deformable linear objects," *IEEE Transactions on Robotics*, vol. 22, no. 4, pp. 625–636, 2006.

[33] P. D. Arendt, D. W. Apley, and W. Chen, "Quantification of Model Uncertainty: Calibration, Model Discrepancy, and Identifiability," *Journal of Mechanical Design*, vol. 134, no. 10, 2012.

[34] C. L. Lei, S. Ghosh, D. G. Whittaker, Y. Aboelkassem, K. A. Beattie, C. D. Cantwell, T. Delhaas, C. Houston, G. M. Novaes, A. V. Panfilov, P. Pathmanathan, M. Riabiz, R. W. dos Santos, J. Walmsley, K. Worden, G. R. Mirams, and R. D. Wilkinson, "Considering discrepancy when calibrating a mechanistic electrophysiology model," *Philosophical Transactions of the Royal Society A: Mathematical, Physical and Engineering Sciences*, vol. 378, no. 2173, p. 20190349, 2020.

[35] D. Ji, T. H. Kang, S. Shim, and J. Hong, "Analysis of Twist Deformation in Wire-driven Continuum Surgical Robot," *International Journal of Control, Automation and Systems*, vol. 18, no. 1, pp. 10–20, 2020.

[36] J. Jung, R. S. Penning, N. J. Ferrier, and M. R. Zinn, "A modeling approach for continuum robotic manipulators: Effects of nonlinear internal device friction," in *IEEE/RSJ International Conference on Intelligent Robots and Systems*, 2011, pp. 5139–5146.